JOURNAL OF AIRCRAFT
Vol. 34, No. 5, September–October 1997

Nonlinear Rotor Aeroelastic Analysis with Stall and Advanced Wake Dynamics

Deman Tang* and Earl H. Dowell†
Duke University, Durham, North Carolina 27708-0300

This paper studies an effective lag damping prediction method for a flexible flap–lag–torsional hingeless rotor model and correlation with the experimental data for a four-bladed rotor. The ONERA dynamic stall models of lift, drag, and pitching moment for each aerodynamic airfoil element and an advanced three-dimensional finite state wake model are used. The nonlinear equations of motion are represented in terms of state variables with 4 × 10 structural state variables. Eight aerodynamic elements for each rotor blade and at least eight wake harmonics are employed. The aerodynamic and wake state variables are 4 × 48 and 45, respectively. A numerical simulation technique is applied to determine the transient response of the hingeless rotor model and to predict the lag damping. Numerical investigations indicate that the present theoretical/numerical method improves the correlation of the theoretical and experimental results compared to an earlier eigenvalue, perturbation analysis.

Nomenclature

a = linear lift curve slope
$a.c$, $e.c$ = aerodynamic center and blade elastic axis
a_e = chord distance between aerodynamic center and blade elastic axis, $1/R$
b = nondimensional blade semichord, $c/2R$
C_d, C_l = airfoil sectional drag and lift coefficient
C_m = airfoil sectional pitch moment coefficient about quarterchord
C_T = thrust coefficient, $1/\rho\pi\Omega^2R^4$
C_{vi}, C_{wi} = ith chord and flap structural damping coefficients
$C_{\phi i}$ = ith torsion structural damping coefficient
c = blade chord
D = section aerodynamic drag force
EI_1 = blade flap bending stiffness
EI_2 = blade chord bending stiffness
e, $\bar{e}$ = mass centroid offset from elastic axis, e/R
e_A = tensile axis offset from elastic axis
e_h = rotor root cuff
GJ = blade torsional stiffness
j, n = polynomial number
K_A = radius of gyration of blade cross section
K_m = mass radius of gyration of blade cross section
k_i = reduced frequency, b/r
L = section aerodynamic lift force
$[L^{c,s}]$ = inflow infuence coefficient mass matrices
L_v, L_w = components of aerodynamic loads per unit length in flap and lag (in-plane) directions
L_0 = apparent mass lift normal to the chord line
L_ϕ = aerodynamic moment per unit length about aerodynamic center
$[M]$ = inflow apparent mass matrices
M_ϕ = aerodynamic moment per unit length about aerodynamic center
m = mass per unit length of the blade
N_a = number of aerodynamic elements
N_b = number of blades
N_s = number of structural degrees of freedom
N_v = number of induced inflow states
R = rotor radius, ft
r = rotor radial distance from the rotating center, $1/R$
t = time, s
$\bar{t}$ = nondimensional time, Ωt
U = section resultant velocity at a blade section, $1/R\Omega$
U_P, U_T = local air velocity components, $1/R\Omega$
V = inflow parameter, $1/R\Omega$
V_i, W_i = generalized coordinates for bending
v_1 = induced inflow velocity, $1/R\Omega$
x = blade radial distance from the root cuff, $1/R$
α = section angle of attack, rad
α_s = shaft tilt angle, positive forward, rad
α_{ss} = quasisteady stall angle, deg
α_j^s, β_j^s = induced inflow expansion coefficients
β_{pc} = precone angle, rad
Γ, Γ_d = lift and drag circulations per length
Γ_m = pitch moment circulation per length
ΔC_d = difference between the extrapolated drag coefficient and measured static value
ΔC_l = difference between the extrapolated lift coefficient and measured static value
ΔC_m = difference between the extrapolated pitch moment coefficient and measured static value
Δ_i = dimensionless width of ith aerodynamic section
ε = airfoil rotation rate with respect to the air mass
θ_e = excitation amplitude angle, rad
θ_s, θ_c = cyclical pitch angle, rad
θ_0 = collective pitch angle, rad, deg
ϑ = normalized eigenvector in torsional direction about the elastic axis of blade
λ_T = total inflow ratio
μ = rotor advance ratio
ρ = air density
σ = damping coefficient of regressing mode in the nonrotating system, s^{-1}
φ, ς = normalized eigenvectors in y and z directions, respectively
τ_n^{mc}, τ_n^{ms} = cosine and sine parts of pressure coefficient
Φ_i = generalized coordinates for torsion
ϕ, v, w = elastic twist about the elastic axis and displacements in the y, z directions
$\phi_j^s(r)$ = radial expansion shape function
ψ_k = azimuth of kth blade
Ω = rotor rotation speed, rad/s

Received Jan. 1, 1997; revision received June 16, 1997; accepted for publication June 16, 1997.

*Research Associate, Department of Mechanical Engineering and Materials Science.

†J. A. Jones Profesor and Dean of the School of Engineering. Fellow AIAA.

ω = nondimensional exciting frequency, $1/\Omega$
ω_{vi}, ω_{wi} = ith nondimensional rotating lag and flap natural frequencies, $1/\Omega$
$\omega_{\phi i}$ = ith nondimensional rotating torsional natural frequency, $1/\Omega$

Subscripts
1, 2 = unstalled and stalled components
ζ, η = ζ and η components

Superscripts
$\dot{}$ = $\mathrm{d}(\ )/\mathrm{d}\bar{t}$
$'$ = $\mathrm{d}(\ )/\mathrm{d}x$

I. Introduction

FINITE state aerodynamic models have proven to be very useful in the nonlinear aeroelastic analysis of rotorcraft. These models are formulated as differential equations in the unknown states of the flowfield, which can then be coupled with a rotor structural model. Numerical solutions of these coupled state equations can be obtained from the Floquet theory when the models are linear, or by time simulation for linear or nonlinear models.

Over the years, many researchers have tried to extend the classical unsteady aerodynamic theories to arbitrary motion in the time domain. Dowell[1] based his theory on a parameter identification technique in which the time history of the aerodynamic load on the airfoil was assumed to consist of sums of exponentials and proposed a procedure for obtaining approximate expressions for Theodorsen's lift deficiency function $C(k)$, and for aerodynamic loads. Dinyavari and Friedmann[2] generalized Loewy's lift deficiency function through a finite state Pade approximation. Dinyavari and Friedmann[3] later presented a more complete derivation of their theory and an incorporation of time domain, arbitrary motion, and unsteady aerodynamics into the nonlinear aeroelastic analysis of a rotor system. Friedmann and Venkatesan[4] further used the Bode plot method to approximate Loewy's lift deficiency function for oscillatory motion.

Even though the preceding finite state models provide an important improvement in the rotor aeroelastic analysis in the time domain, these models still do not give a rigorous state representation in forward flight.[5] Thus, Peters and He[6] proposed a three-dimensional dynamic wake model.[6] This aerodynamic model is derived from potential flow theory with no restrictive assumptions on the time history of airfoil motions. The aerodynamic states represent the induced flow that are expressed in terms of a Fourier series azimuthally, and a polynomial distribution radially, on the rotor disk. This aerodynamic model is constructed as a set of first-order state equations and is easily coupled to the corresponding structural equations.

An effective lag damping prediction method,[7,8] using a simpler wake model, has been applied to stalled rotor flap–lag–torsional stability investigations, and the results have been compared with the experimental data provided by McNulty[9] and Maier et al.[10] The purpose of the present work is to extend the preceding lag damping prediction by using a higher order unified ONERA aerodynamic stall[11,12] and a finite state dynamic wake model developed by Peters and He.[6] The equations of motion for the elastic bending and torsion of a nonuniform rotor blade are based on the Hodges and Dowell equations.[13] The nonlinear equations of motion are represented in terms of state variables with 4×10 structural state variables. Eight aerodynamic elements for each rotor blade and eight wake harmonics for the wake model are required for a converged wake representation. The number of aerodynamic and wake state variables are 4×48 and 45, respectively.

A direct numerical time-marching integration is used to compute the transient response (free oscillation) of the flap–lag–torsional motion of the rotor. A periodic pitch oscillation is added to the nonlinear state equation to simulate the conventional swashplate of the experiment. The driving frequency is set equal to the value that was used in the experiment, and the oscillation amplitude is used as a control input parameter. When the blade motion reaches a steady state, the additional pitch excitation is removed. The subsequent lag response provides good transient data. A time-domain quasilinear model identification technique is applied to identify the damping and frequency for the regressing mode. A typical forward-flight numerical example and correlation with the experimental results are provided.

The experimental rotor is trimmed by minimizing the root flap moment at 12% radius through adjusting the collective pitch, longitudinal, and lateral cyclic pitch angles. In the present numerical prediction, the external trim conditions (cyclical control angles, θ_s, θ_c, and collective pitch angle θ_0) are taken to be the experimental values. The present results are also compared with previous results[8] obtained using simpler wake models, i.e., Pitt and Peters' 3×3 dynamic inflow model and a uniform inflow model.[14]

II. Equations of Motion

A. Nonlinear Structural Equations

The present numerical study is based upon an isolated, hingeless rotor model with coupled bending/torsional motion.[10] The experimental model consists of four flexible rotor blades. The soft in-plane rotor system was designed with low torsional stiffness to emphasize the effects of torsion. The rotor is trimmed with cyclic pitch. For a given advance ratio, the collective pitch and shaft tilt angles are the specified control input parameters. The basic equations of motion for the elastic bending and torsion of the nonuniform rotor blade are based on the Hodges and Dowell equations.[13] The cross-sectional warping and higher-order nonlinear terms are neglected consistent with the design of the experimental model. Three nonlinear partial differential equations for v, w, and ϕ are obtained, and the equation for the radial elastic displacement u, is eliminated from above three equations. The terms $u' + (v'^2/2) + (w'^2/2)$ and u are expressed in terms of v, w, and ϕ only.[13]

Expansions in general mode shape functions are used to obtain ordinary differential equations (ODEs) in terms of generalized coordinates. They are expressed in series form as follows:

$$v = \sum_{j=1}^{N} V_j(t)\varphi_j(x)$$

$$w = \sum_{j=1}^{N} W_j(t)\varsigma_j(x) \tag{1}$$

$$\phi = \sum_{j=1}^{N} \Phi_j(t)\vartheta_j(x)$$

where V_j, W_j, Φ_j, and x are nondimensionalized with respect to the blade span, R. φ_j, ς_j and ϑ_j and the jth normal modes of the associated linear problem in the rotational system.

Using the Galerkin method a set of nondimensional equations are obtained. The velocity, acceleration, and natural frequency terms are nondimensionalized by $R\Omega$, $R\Omega^2$, and Ω, respectively,

$$\ddot{V}_i + C_{vi}V_i + \omega_{vi}^2 V_i + 4\sum_{j=1}^{N} v_{1ij}\ddot{V}_j + 2\sum_{j=1}^{N} v_{2ij}\dot{V}_j$$

$$- 2\beta_{pc}\sum_{j=1}^{N} v_{3ij}W_j + N_v = \gamma_{vi}\int_0^1 \varphi_i L_v \,\mathrm{d}x \tag{2}$$

$$\ddot{W}_i + C_{wi}W_i + \omega_{wi}^2 W_i + \sum_{j=1}^{N} w_{1ij}\ddot{\Phi}_j + 2\beta_{pc}\sum_{j=1}^{N} w_{2ij}V_j + \sum_{j=1}^{N} w_{3ij}\Phi_j + N_w = \gamma_{wi}\int_0^1 \varsigma_i L_w \, dx - w_{4i}\beta_{pc} \tag{3}$$

$$\ddot{\Phi}_i + C_{\phi i}\Phi_i + \omega_{\phi i}^2\Phi_i + \sum_{j=1}^{N} p_{1ij}\ddot{W}_j + \sum_{j=1}^{N} p_{2ij}W_j + N_\phi = \gamma_{\phi i}\int_0^1 \vartheta_i M_\phi \, dx - p_{3i}\beta_{pc} \tag{4}$$

where

$$N_v = 2\sum_{j=1}^{N}\sum_{k=1}^{N} v_{5jk}^i(W_j\Phi_k + W_j\Phi_k) + 2\sum_{j=1}^{N}\sum_{k=1}^{N} v_{6jk}^i V_j V_k - 2\sum_{j=1}^{N}\sum_{k=1}^{N} v_{7jk}^i W_j W_k + \sum_{j=1}^{N}\sum_{k=1}^{N} v_{8jk}W_j\Phi_k$$

$$N_w = \sum_{j=1}^{N}\sum_{k=1}^{N} w_{5jk}^i V_j\Phi_k + 2\sum_{j=1}^{N}\sum_{k=1}^{N} w_{6jk}^i V_j\Phi_k + 2\sum_{j=1}^{N}\sum_{k=1}^{N} w_{7jk}^i V_j W_k$$

$$N_\phi = \sum_{j=1}^{N}\sum_{k=1}^{N} p_{5jk}^i V_j W_k - \sum_{j=1}^{N}\sum_{k=1}^{N} p_{6jk}^i V_j\Phi_k + 2\sum_{j=1}^{N}\sum_{k=1}^{N} p_{7jk}^i V_j\Phi_k + 2\sum_{j=1}^{N}\sum_{k=1}^{N} p_{8jk}^i V_j W_k$$

The coefficients, v_{1ij} . . . , w_{1ij} . . . , and p_{1ij} . . . are given in the appendix of Ref. 8.

The structural state variable equation is expressed as a nonlinear matrix equation of first order:

$$[A_s]\{\boldsymbol{q}_s\} = [B_s]\{\boldsymbol{q}_s\} + \{\boldsymbol{F}_s\} \tag{5}$$

where $\boldsymbol{F}_s$ is the vector of nonlinear forces caused by the nonlinear terms in the original differential equations of motion, and

$$\{\boldsymbol{q}_s\}^T = \lfloor W_j W_j V_j V_j \Phi_j \Phi_j \rfloor \tag{6}$$

B. Stall Aerodynamic Equations

The aerodynamic forces, L_v, L_w, and M_ϕ, are based on the ONERA dynamic stall models of unsteady unified lift, drag, and pitching moment, which are virtually independent. With Γ, Γ_d, and Γ_m representing the instantaneous circulation providing lift, drag, and pitch moment, respectively, the full dynamic stall models are represented as follows.

Dynamic stall lift:

$$\Gamma = \Gamma_1 + \Gamma_2 \qquad \Gamma_1 = aU_\zeta\cos\alpha + \delta_l b\varepsilon$$

$$k^2\ddot{\Gamma}_2 + 2\,\mathrm{d}wk\dot{\Gamma}_2 + w^2(1+d^2)\Gamma_2 = -w^2(1+d^2)\left[U\Delta C_l + e_l k(U_\eta\cos\alpha + U_\zeta\sin\alpha)\Delta C_l + e_l k\frac{\partial\Delta C_l}{\partial\alpha}(U_\zeta\cos\alpha - U_\eta\sin\alpha)\right] \tag{7}$$

Dynamic stall drag:

$$\Gamma_d = \Gamma_{d1} + \Gamma_{d2} \qquad \Gamma_{d1} = UC_{d0}$$

$$k^2\ddot{\Gamma}_{d2} + a_d k\dot{\Gamma}_{d2} + r_d^2\Gamma_{d2} = -\left[r_d^2 U\Delta C_d + e_d k\left(U_\eta\Delta C_d + \frac{\partial\Delta C_d}{\partial\alpha}U_\zeta\right)\right] \tag{8}$$

Dynamic stall pitching moment:

$$\Gamma_m = \Gamma_{m1} + \Gamma_{m2} \qquad \Gamma_{m1} = \delta_m b\varepsilon$$

$$k^2\ddot{\Gamma}_{m2} + 2\,\mathrm{d}wk\dot{\Gamma}_{m2} + w^2(1+d^2)\Gamma_{m2} = -w^2(1+d^2)\left[U\Delta C_m + e_m\mathrm{k}(U_\eta\cos\alpha + U_\zeta\sin\alpha)\Delta C_m + e_m k\frac{\partial\Delta C_m}{\partial\alpha}(U_\zeta\cos\alpha - U_\eta\sin\alpha)\right] \tag{9}$$

where Γ_1, Γ_2, Γ_{d1}, Γ_{d2}, Γ_{1m}, and Γ_{2m} represent lift, drag, and pitching moment circulations per length for the linear and stalled contribution, respectively. The differential operator is relative to the rotor azimuth angle (d/dψ), and an average dimensionless reduced frequency ($k = \Omega b/U_0 = b/r$) is used in this paper. ε is the airfoil rotation rate with respect to the air mass, which includes all geometric rotations of the blade aerodynamic element. For the present rotor blade motion, $\varepsilon = \dot{\theta} + (1 + v/r)\sin(w/r)$. Δ_l, ΔC_d, and ΔC_m are the differences between the extrapolated linear lift, drag, and pitching moment coefficients and quasisteady stall coefficients in the stalled region, respectively. The aerodynamic coefficients are given in the appendix of Ref. 7 for a NACA 0012 section.

The stall aerodynamic pitching moment coefficient may be important for a rotor blade of low torsional stiffness. In the present calculations, we assume that the stall pitching moment coefficient behaves similarly to the stall lift coefficient. For the NACA 0012 airfoil, this assumption is in reasonable agreement with the experiment.[15]

The aerodynamic state variable equations is expressed as a nonlinear matrix equation of first order:

$$[A_a]\{\boldsymbol{q}_a\} = [B_a]\{\boldsymbol{q}_a\} + \{\boldsymbol{F}_a\} \tag{10}$$

where $\boldsymbol{F}_a$ is the vector of nonlinear aerodynamic forces and

$$\{\boldsymbol{q}_a\}^T = \lfloor \Gamma_{2i}\dot{\Gamma}_{2i}\Gamma_{d2i}\dot{\Gamma}_{d2i}\Gamma_{m2i}\dot{\Gamma}_{m2i}\rfloor \tag{11}$$

C. Relationship Between Aerodynamic Forces and Flow Velocities

From kinematics (Fig. 1), the resultant velocity U and the angle of attack α are given by

$$U = \sqrt{U_P^2 + U_T^2} = \sqrt{U_\zeta^2 + U_\eta^2}$$

where

$$U_T = v + r\cos(w') + \mu\sin(\psi + v/r) \tag{12}$$

$$U_P = w + \mu\cos(\psi + v/r)\sin(w') - \lambda_T\cos(w') \tag{13}$$

$$\lambda_T = \mu\tan\alpha_s + v_1(r, \psi, \bar{t})$$

$\mu\tan\alpha_s$ is the axial component of the freestream, and $v_1(r, \psi, \bar{t})$ is the induced inflow distribution at the rotor disk. For details, see Sec. II.D. Now,

$$\alpha = \tan^{-1}(U_\zeta/U_\eta) \tag{14}$$

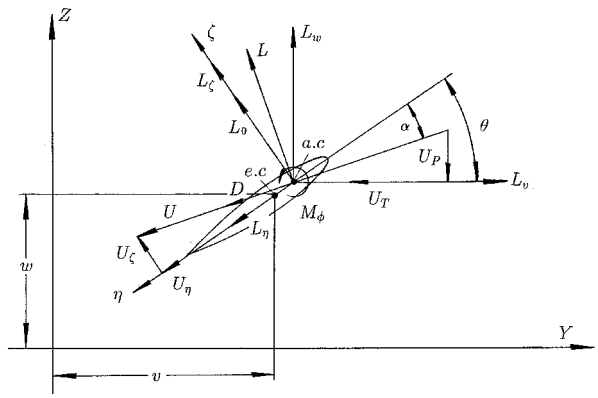

Fig. 1 Sectional aerodynamic forces and velocities.

where

$$U_\eta = U_T\cos\theta + U_P\sin\theta \qquad U_\zeta = U_T\sin\theta - U_P\cos\theta$$

$$\theta = \theta_0 + \theta_s\sin\psi + \theta_c\cos\psi + \hat{\phi} + \theta_e\sin\omega t\sin\psi \tag{15}$$

$$\hat{\phi} = \phi - \int_0^x v''w'\,dx$$

The cyclic pitch angles θ_s and θ_c are experimentally determined from the trim conditions, which depend upon μ, α_s, and θ_0. The values are given in Ref. 10. In the dynamic stability testing, an external excitation provided a cyclic excitation at the regressing lag mode frequency. To accomplish this, a hydraulic actuator was used to drive the swashplate with θ_e and ω. To simulate the experimental excitation condition, an external pitch excitation $\theta_e \sin\omega\sin\psi$ is added to Eqs. (2–4). The exciting frequency includes two frequency components, $\Omega - \omega$ and $\Omega + \omega$, in the rotating system, and three frequency components, $2\Omega + \omega$, $2\Omega - \omega$, and ω, in the nonrotating system. If $\omega = 0.29$ is chosen, i.e, the test value, 8.4 Hz, then an exciting frequency, 0.71, in the rotating system and 0.29 in the nonrotating system is obtained. The first lag natural frequency of the experimental rotor is 0.71 and the regressing lag mode frequency is 0.29.

The ONERA dynamic stall model is based on a blade airfoil element. Here, it is applied to a single flexible bending/torsion blade motion. A simple assumption is that the blade is divided into N_a spanwise sections and the ONERA model is applied to each section. The aerodynamic forces for a generic ith blade aerodynamic element can be expressed as

$$L_{wi} = [U_T\Gamma - U_P\Gamma_d + L_0\cos\theta]_i \tag{16}$$

$$L_{vi} = -[U_P\Gamma + U_T\Gamma_d + L_0\sin\theta]_i \tag{17}$$

$$M_{\phi i} = [2bU\Gamma_m + M_0 + aeL_\zeta]_i \tag{18}$$

where

$$L_{\zeta i} = [U_\eta\Gamma + U_\zeta\Gamma_d + L_0]_i$$

$$L_{0i} = [bs_l U_\zeta]_i$$

$$M_{0i} = [bs_m U_\zeta]_i$$

Substituting Eqs. (16–18) into the right-hand side of Eqs. (2–4), a set of the second-order ODEs in the structural variables W_j, V_j, and Φ_j, and aerodynamic variables Γ_i, Γ_{di}, Γ_{mi} are obtained. Two N_s state variables each are required for the structural degrees of freedom (flapping, lag, and torsion motions). Equations (7–9) represent a third- and second-order system, respectively. Thus, six state variables are required per section for each equation. Combining Eqs. (5) and (10), a set of $6N_a + 2N_s$ nonlinear first-order differential equations is obtained.

Note that the velocity components U_P and U_T involve the state variables w_j, v_j, and ϕ_j. Equations (5) and (10) are a set of nonlinear differential equations whose solution can be obtained by numerical time integration. The initial values of U_P and U_T are determined by the initial values of the state variables.

D. Equations of Motion with Peters' Dynamic Wake Model

From Ref. 6, the induced flow v_1 at the rotor disk can be represented by

$$v_i(r,\psi,\bar{t}) = \sum_{s=0}^{\infty}\sum_{j=s+1,s+3,\ldots}^{\infty}\phi_j^s(r)[\alpha_j^s(\bar{t})\cos(s\psi) + \beta_j^s(\bar{t})\sin(s\psi)] \tag{19}$$

and the generalized dynamic wake equations can be expressed in the following form:

$$[M]\{\dot{\alpha}_j^s\} + V[L^c]^{-1}\{\alpha_j^s\} = \tfrac{1}{2}\{\tau_n^{mc}\} \tag{20}$$

$$[M]\{\dot{\beta}_j^s\} + V[L^s]^{-1}\{\beta_j^s\} = \tfrac{1}{2}\{\tau_n^{ms}\} \tag{21}$$

where V is an inflow parameter to account for energy added to the flow from the rotor, which is given by

$$V = \frac{\mu^2 + \lambda(\lambda + \lambda_m)}{\sqrt{\mu^2 + \lambda^2}}$$
$$\lambda = \mu\tan\alpha_s + \lambda_m \tag{22}$$

where λ_m is the momentum-theory value of steady induced flow for a trimmed rotor

$$\lambda_m = (2/\sqrt{3})\{1\ 0\ 0\ \ldots\}[L^c]^{-1}\{\alpha_n^m\}$$

This makes the dynamic wake equations nonlinear through the dependence of V upon the states α_n^m. Also, the induced inflow influence coefficient matrices $[L^c]$ and $[L^s]$ depend upon the effective disk angle of attack and, thus, the states α_n^m. For the coefficients of Eqs. (19–21), see Ref. 6.

For rotors with a finite number of blades, the pressure across the disk can be approximately represented as a lifting line for each blade by the following instantaneous functions of the blade loading L_w:

$$\tau_n^{0m} = \frac{1}{2\pi}\sum_{k=1}^{4}\int_{e_h}^{1}\phi_n^0(r)(L_w)_k\,dr$$
$$\tau_n^{mc} = \frac{1}{\pi}\sum_{k=1}^{4}\int_{e_h}^{1}\phi_n^m(r)(L_w)_k\cos(m\psi_k)\,dr \tag{23}$$
$$\tau_n^{ms} = \frac{1}{\pi}\sum_{k=1}^{4}\int_{e_h}^{1}\phi_n^m(r)(L_w)_k\sin(m\psi_k)\,dr$$

Because of the different inflow velocities on each rotor blade, the individual blade motions and corresponding aerodynamic circulations have to be taken as independent degrees of freedom. Hence, $\bar{t}$, $\{q_s\}$, and $\{q_a\}$ are defined by $\psi_k = \bar{t} + 2\pi(k-1)/4$, $\{q_s\}_k$, and $\{q_a\}_k$, where k denotes an individual blade. Thus, for a rotor system with four blades and for a dynamic wake model with N_v degrees of freedom, the resulting system of state variable equations is expressed as a nonlinear matrix equation of first order:

$$[A]\{\dot{q}\} = [B]\{q\} + \{F_N\} \tag{24}$$

where $\boldsymbol{F}_N$ is the vector of nonlinear forces caused by the nonlinear terms in the original differential equations of motion, and

$$\{\boldsymbol{q}\}^T = \lfloor (q_s)_k,\ (q_a)_k,\ q_\lambda \rfloor \tag{25}$$

where

$$\{\boldsymbol{q}_\lambda\}^T = \lfloor \alpha_j^s \beta_j^s \rfloor$$

The matrix $[B]$ involves the induced inflow influence coefficient matrices $[L^{c,s}]$ and the flow parameter V. Thus, $[B]$ is a function of the inflow state variable q_λ, and is updated at each numerical integration time step.

The structural and aerodynamic state variables are $2 \times N_b \times N_s$ and $6 \times N_b \times N_a$, respectively. The total degrees of freedom of this system are $N_b \times (2N_s + 6N_a) + N_v$. For the present numerical investigation, we use $N_b = 4$, $N_a = 8$, $N_v = 45$, and $N_s = 5$ (two flapping modes, two lag modes, and one torsion mode).

III. Lag Damping and Solution Procedure

In this paper, we use direct numerical time integration to compute the transient response (free oscillation) of the flexible rotor blade motion. As in the experimental excitation, a periodic pitch excitation is added to the pitch variable θ of Eqs. (2–4). The driving frequency is set equal to the first regressing mode frequency. The force magnitude is used as a control input parameter. When the blade motion reaches a steady state, the additional pitch excitation is removed. The subsequent dominant lag response provides good transient data, primarily in the lag mode. For the in-plane stability analysis of the flexible rotor, the damping and frequency for the regressing mode in the nonrotating system are of primary concern, and this approach tends to lead to excitation and response in essentially a single mode. Also, this method of excitation most closely responds to the way in which the experimental data were obtained.[10] A time-domain quasilinear model identification (ITD) is applied to identify the damping and frequency for the global regressing mode, as was done in Ref. 10.

The numerical calculation needs an initial inflow value $\bar{\alpha}_1^0$. At the start of the calculation, we assume the inflow to be a steady uniform induced flow; thus, it is determined by a rotor momentum theory.

The numerical investigation has focused on the prediction of lag damping for the global regressing mode in forward flight, based on the full Peters' unified ONERA dynamic stall and wake models. The parameters of the experimental model rotor of Ref. 10 are used in the present computation including two flap, two lag, and one torsion modes. The blade is divided into eight spanwise aerodynamic elements starting from $r = 0.215$. The flexure section of the blade ($r = 0.104$–0.215) is assumed to be a no lift or pitch moment section because of the rectangular airfoil section, and the aerodynamic drag is neglected. The wake harmonic number is taken as 8 with 45 inflow states. The measured structural modal damping of $\xi_w = \xi_\phi = 0.01$, and $\xi_v = 0.005$ was included in the analysis. The natural frequencies and modes of the rotor system are calculated using a finite element method. The frequencies for the nominal rotor speed of 1700 rpm were compared with calculations from the comprehensive analytical model of rotorcraft aerodynamics and dynamics, Johnson Aeronautics version (CAMRAD/JA). There is good agreement between the two theoretical predictions.[8]

The experimental rotor is trimmed by minimizing the root flap moment at 12% radius through adjusting the collective pitch, longitudinal, and lateral cyclic pitch angles, and a theoretical prediction of the root flap moment is made. In a rotating system, the flap moment at the blade root at 12% radius is determined by integrating Eq. (3) from $r = 0.12$ to $r = 1$ over one cycle when the rotor blade motion reaches a steady state under zero initial conditions.

IV. Numerical Results and Comparison with Experiment

A. Regressing Lag Damping

Following the work of Ref. 8, only the forward-flight case for $\theta_0 = 3$ deg is discussed. In this case, Eq. (24) includes 40 DOFs for the structural motion (the first two flaps, lag modes, and the fundamental torsional mode), 192 DOFs for the aerodynamic blade model, and 45 DOFs for the wake inflow. In the numerical simulation, 180 revolutional cycles with the integral step length, $2\pi/120$, were calculated. A typical blade lag response curve for $\alpha_s = -3$ deg and $\mu = 0.15$ is shown in Fig. 2. The first 60 revolutional cycles are the transient response under zero initial conditions. The blade motion reaches a steady state after 40 cycles, which is called the trimmed condition of this system. At $\bar{t}/2\pi = 61$ cycles, the external excitation with lag angle $\theta_e = 0.5$ deg, $\omega = 0.29$ is added into this system. As shown in Fig. 2, the process from $\bar{t}/2\pi = 61$ to 120 cycles is steady forced oscillation. At $\bar{t}/2\pi = 121$ cycles, the external excitation is removed, and the transient response data are obtained for the duration of 60 cycles. The response decays with time, and the decay rate depends on the system damping. The transient response included the dominant component with frequency of the regressing mode 8.4 Hz, and higher order components with frequency 1.71Ω. A typical regressing lag transient response time history from $\bar{t}/2\pi = 121$ to 180 revolution cycles for $\mu = 0.15$ and $\alpha_s = -3$ deg is shown in Fig. 3. We have used an ITD computational code[7] to determine the lag damping and frequency. For convenience in the ITD analysis, the nondimensional time is returned to real time, and the starting time is set to zero (Fig. 3). From this figure, it is found that the regressing mode frequency component (8.4 Hz) is dominant and the higher-order components are small. Corresponding to the dominant frequency component, the regressing lag damping is 0.92 from the ITD analysis. From the calculations, it is also found that the lag damping values from the individual rotor blades are the same as the global value. This is different from the experiment, and per-

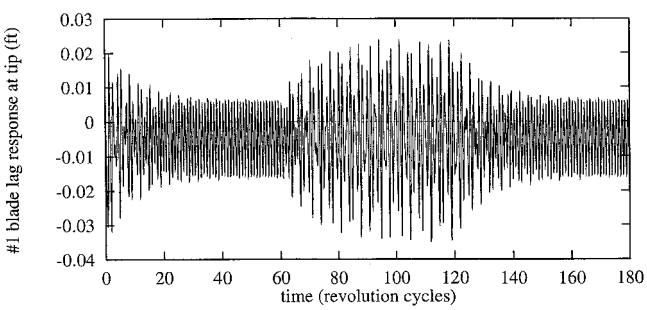

Fig. 2 Number 1 blade lag response time history for $\alpha_s = -3$ deg and $\mu = 0.15$.

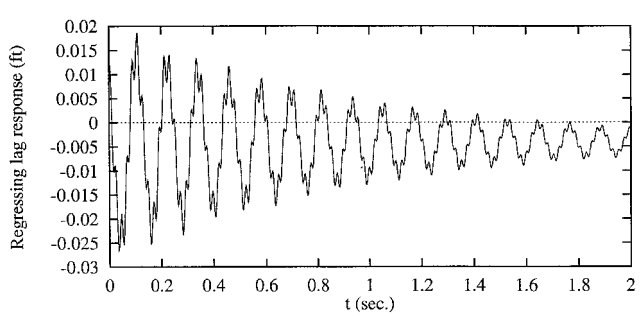

Fig. 3 Transient time histories of the regressing mode from numerical simulation for $\alpha_s = -3$ deg and $\mu = 0.15$.

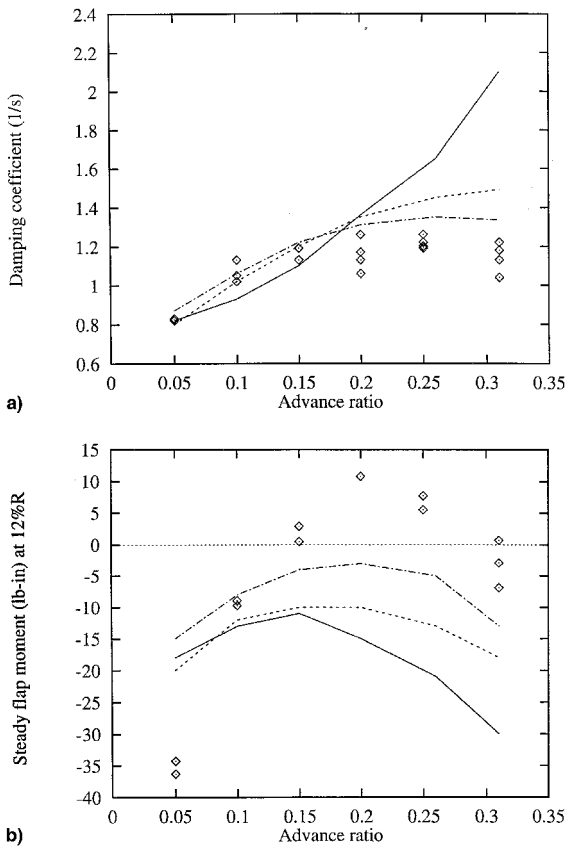

Fig. 4 a) Forward-flight regressing lag mode damping and b) steady root flap moment vs advance ratio for collective pitch θ_0 = 3 deg, α_s = 0 deg: the solid line is from the uniform inflow, the broken line is from the 3 × 3 dynamic inflow, the dot–dash line is from the present method, and ◇ is from measured data.

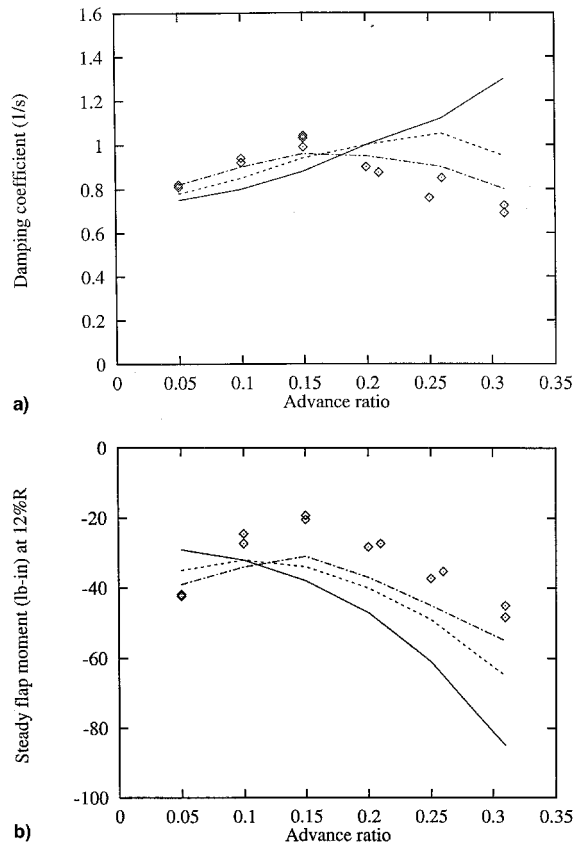

Fig. 5 a) Forward-flight regressing lag mode damping and b) steady root flap moment vs advance ratio for collective pitch θ_0 = 3 deg.

haps suggests that blade-to-blade differences may have been important in the experiment.

Figures 4a, 5a, and 6a show the regressing lag damping vs μ, for θ_0 = 3 deg, with α_s = 0, −3, and −6 deg, respectively. A comparison between the theory and experiment is also shown in these figures. In Figs. 4a, 5a, and 6a, the solid and broken lines indicate the results from the uniform inflow and Pitt and Peters' 3 × 3 dynamic inflow models,[14] respectively. The dot–dash line is the present analysis results from the advanced wake model. The advanced dynamic wake model improves significantly the theoretical/experimental correlation over Pitt and Peters' early 3 × 3 dynamic inflow model,[14] and also the simplified uniform inflow model, particularly in the range of the higher advance ratio. It is interesting to find that at higher α_s and μ, such as α_s = − 6 deg and $\mu > 0.2$, the present theoretical results are closer to the experimental data than those at lower α_s and μ. From these results, it is concluded that the combination of the ONERA stall model and a more advanced Peters and He's wake model[6] is an important factor for improving the correlation with experimental data.

Figure 7 shows the mean thrust value $\bar{C}_T$ vs the cyclic number for the transient process when μ = 0.26 and α_s = − 6 deg. The mean thrust is equivalent to an average of the lift over the rotor disk. The external cyclic excitation is removed starting from the $\bar{t}/2\pi$ = 121 revolutional cycles. $\bar{C}_T$ is calculated by

$$\bar{C}_T \cong 2\sqrt{3}\bar{\alpha}_1^0\sqrt{\mu^2 + \lambda^2}$$

From Fig. 7, it is found that the mean thrust is an oscillatory decaying motion with time. The oscillation frequency is about 0.29, which equals the regressing frequency in the non-rotating system. When the transient process completely disappears, the average thrust attains a constant value. The decay behavior depends on the system damping.

B. Root Flap Moment

The collective pitch, longitudinal, and lateral cyclic pitch angles are used to minimize the root flap moment at 12% for trimming this rotor system. To assess the accuracy and computational efficiency of the present method, we examined the 1/rev root flap moment at 12% R for correlation with the experimental data. As shown in Fig. 2, the trim condition is reached after 40 revolution cycles. We take one cycle of data in the trim state to calculate the steady root flap moment (time-averaged value). The total root flap moment is determined by the force-integration approach of the aerodynamic lift and the inertial moments (including contributions from centrifugal forces). The results are shown in Figs. 4b, 5b, and 6b for the same conditions as in Figs. 4a, 5a, and 6a. From these figures, it is found that the measured and calculated root flap moment match reasonably well. The results also demonstrate the combination of dynamic stall, and an advanced wake model improves the trim correlation with experimental data. The damping prediction for hingeless rotor aeroelastic stability must consider the rotor trim condition.

A set of the steady blade flap response curves over one revolution cycle is shown in Fig. 8 for α_s = −6 deg and several advance ratios. The motion is represented by the blade tip amplitude (feet), and the response is periodic with a dominant frequency determined by the rotating speed of the rotor. In Fig. 8, the solid, broken, and dot–dash lines indicate the results from μ = 0.31, 0.2, and 0.1, respectively. As μ increases, the blade flap response amplitude increases. This leads to a larger root flap moment for larger μ, as shown in Fig. 6b.

To assess the effect of the stall model on the lag damping and the steady flap moment, we compare predictions with and without this stall model. As an example, Figs. 6c and 6d show

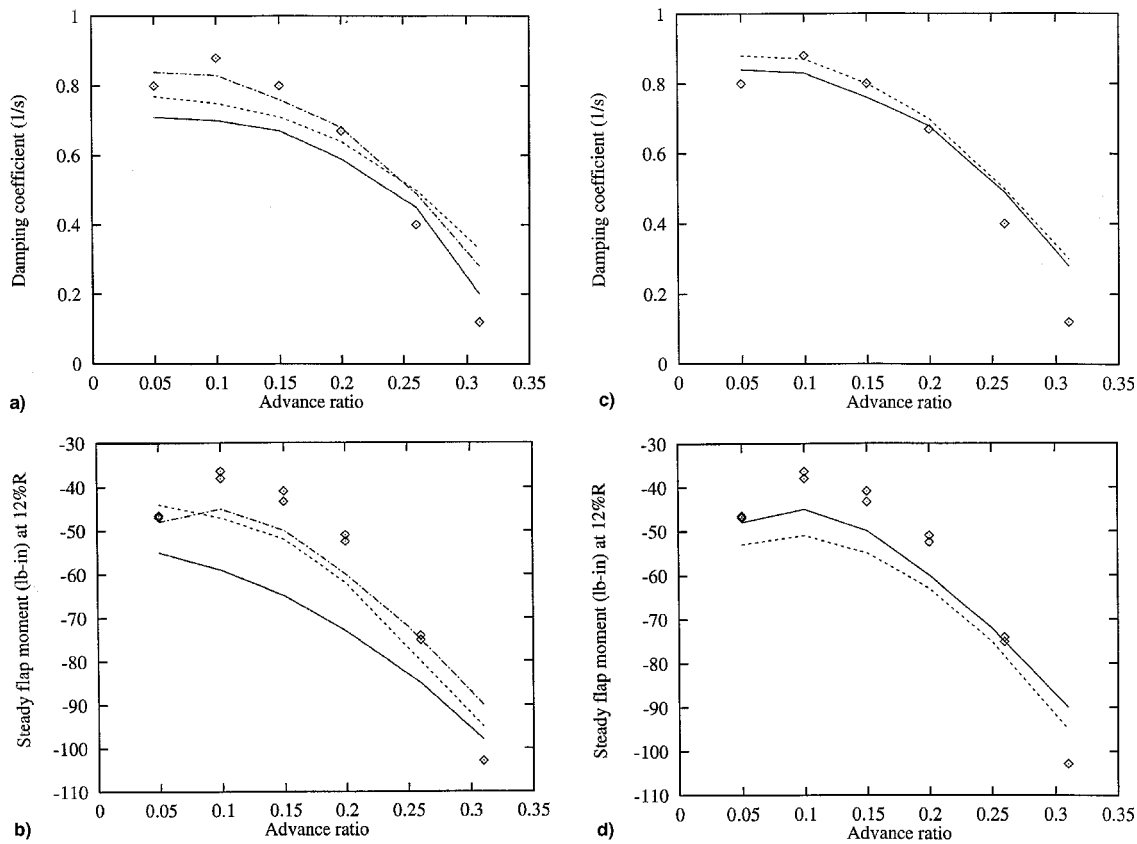

Fig. 6 a), c) Forward-flight regressing lag mode damping and b), d) steady root flap moment vs advance ratio for collective pitch θ_0 = 3 deg, $\alpha_s = -6$ deg. For c), d), the solid line is from the present method with stall model, the broken line is from the present method without stall model, and ◇ is from measured data.

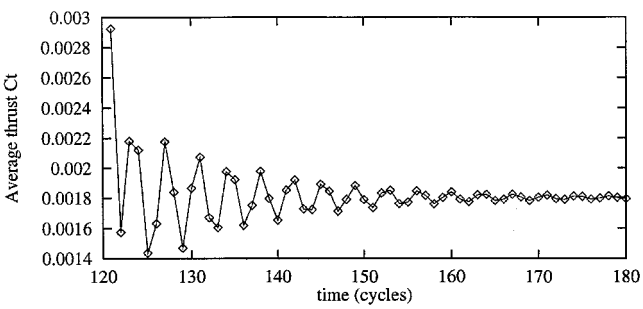

Fig. 7 Average thrust $\bar{C}_T$ vs the cyclic number for $\alpha_s = -6$ deg and $\mu = 0.26$ in the transient process.

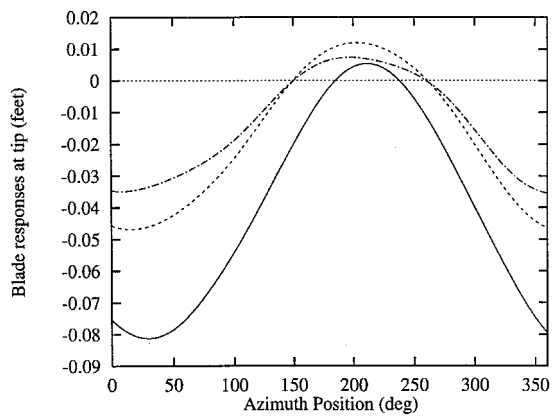

Fig. 8 Steady blade flap response curves vs several advance ratios over one revolution cycle for $\alpha_s = -6$ deg: the solid line is from $\mu = 0.31$, the broken line is from $\mu = 0.2$, and the dot–dash line is from $\mu = 0.1$.

the regressing lag damping and the steady root flap moment vs μ, for $\theta_0 = 3$ deg and $\alpha_s = -6$ deg, respectively. The solid and broken lines indicate the results using the advanced wake model with and without the stall model, respectively; ◇ represents measured data. It is found the effect of the stall is not significant because of good trim condition. This result is also expected from the contour plots for the angle-of-attack distribution as shown in Fig. 9. The stall region occupies a small portion of the rotor disk, and the contribution of lift stall to the root flap moment is correspondingly small.

C. Induced Inflow Distribution

For further insight into the effects of the dynamic wake model on rotor aeroelastic stability, the time-averaged induced inflow distribution over one rotor revolution in the steady trim conditions is considered. In equation (19), the induced flow state variables are taken as the time-averaged values over one cycle. Therefore, the induced inflow v_1 only depends upon the blade radial and azimuthal locations. Figure 10 presents contour plots of the induced-inflow distribution for $\alpha_s = -6$ deg: Fig. 10a, $\mu = 0.1$; Fig. 10b, $\mu = 0.2$; and Fig. 10c, $\mu = 0.31$. The view in Fig. 10 is from above the rotor looking down on the rotor disc. The freestream is from left to right (as indicated by the arrow) and the direction of rotor rotation is counterclockwise. The contour interval is $\Delta\bar{v}_1 = 0.005$. From Fig. 10a, for $\mu = 0.1$, we see that the induced inflow is asymmetrical about the longitudinal centerline of the rotor. The time-averaged induced inflow varies from -0.05 to 0.06. The largest downwash occurs in the rear portion of the disc, i.e., near $\psi = 270-360$ deg and the blade tip. The largest negative induced inflow occurs in the front portion of the disc near the blade tip and $\psi = 180$ deg. At the blade root, the induced inflow is almost zero. The induced inflow increases with moving the radial position from the root to the tip of the blade for each

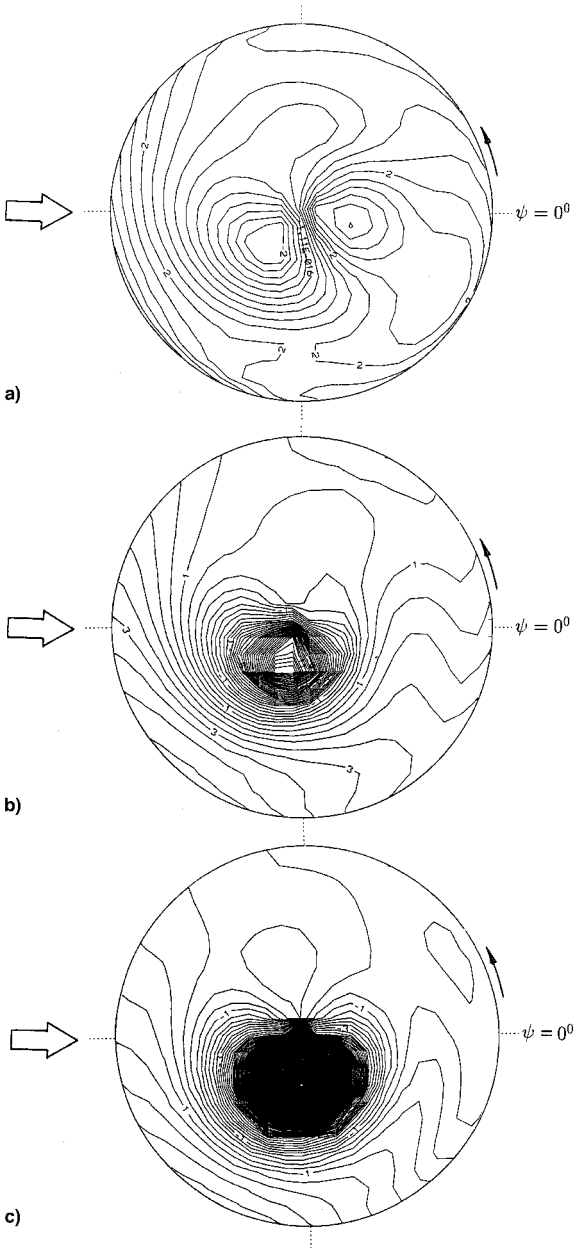

Fig. 9 Contour plots for the angle of attack distribution for α_s = −6°: from μ = a) 0.1, b) 0.2, and c) 0.31.

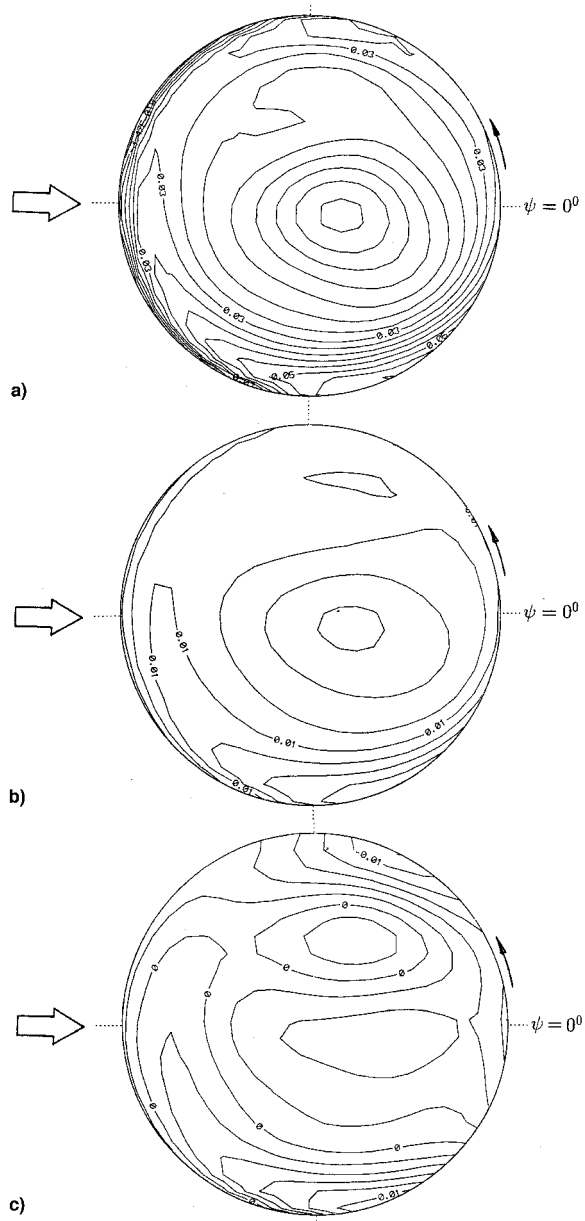

Fig. 10 Time-averaged countour plots for the induced-inflow distribution for α_s = −6 deg: from μ = a) 0.1, b) 0.2, and c) 0.31.

azimuthal position. For μ = 0.2, as shown in Fig. 10b, the time-averaged induced inflow decreases from 0.06 of μ = 0.1 to 0.04. The largest downwash also occurs in the range of ψ = 270−360 deg and at the blade tip. The largest negative induced inflow −0.01 occurs in the front portion of the disc near the blade tip. The asymmetry about the longitudinal centerline of the rotor is stronger than for μ = 0.1. As shown in Fig. 10c, the largest time-averaged induced inflow drops from 0.06 for μ = 0.1 to 0.01 for μ = 0.31. The contour interval is $\Delta\bar{v}_1$ = 0.002. The largest downwash occurs near ψ = 315 deg and the blade tip. The asymmetry about the longitudinal centerline of the rotor is more pronounced.

D. Angle-of-Attack Distribution

The angle-of-attack distribution over one rotor revolution in the steady trim conditions is discussed. From Eq. (14), the angle of attack varies with both radial and azimuthal positions. Contour plots are shown in Fig. 9 for α_s = −6 deg; Fig. 9a, μ = 0.1; Fig. 9b, μ = 0.2; and Fig. 9c, μ = 0.31. The contour plot structure is the same as in Sec. IV.C. The contour interval is $\Delta\alpha$ = 0.4 deg. From Fig. 9a, for μ = 0.1, we see the angle-of-attack distribution is in a linear range. The angle of attack varies from −2.4 to 6.19 deg. In this case, a quasisteady aerodynamic theory can be used with sufficient accuracy. The distribution is asymmetrical about the longitudinal centerline of the rotor. For μ = 0.2, as shown in Fig. 9b, the angle of attack varies from −14 to 5 deg. The largest angle of attack occurs near the blade root area of r < 0.4 and ψ = 180−360 deg. A slight stall occurs near this area, but the effects of dynamic stall can be neglected. The asymmetry about the longitudinal centerline of the rotor becomes stronger than that for μ = 0.1. For μ = 0.31, as shown in Fig. 9c, the angle of attack varies from −150 to 3.7 deg. The largest angle of attack occurs near the blade root area when r < 0.5 and ψ = 180−360 deg, and the area is enlarged. A stronger stall occurs near this area and the effects of dynamic stall must be considered. Also, the asymmetry about the longitudinal centerline of the rotor becomes stronger than that for μ = 0.2. From Fig. 9, it is found most of the lift area of this rotor is not in the aerodynamic stall range. This is because this rotor is trimmed by adjusting collective pitch, longitudinal, and lateral cyclic pitch angles in the experimental model.

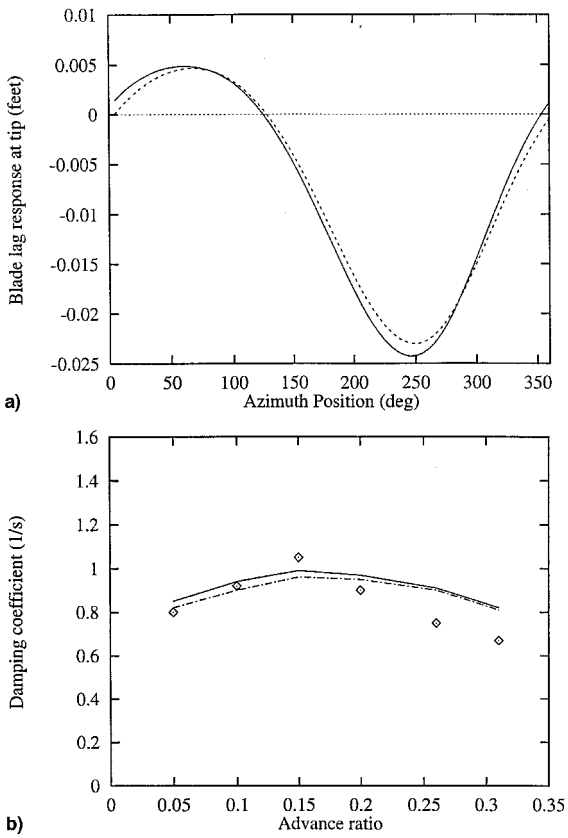

Fig. 11 Blade lag response and regressing lag damping for comparing the influence of the nonlinear term, $[L^{c\text{-}s}]^{-1}$: a) blade lag response for $\alpha_s = -3$ deg and $\mu = 0.26$ and b) regressing lag damping vs advance ratio for $\alpha_s = -3$ deg.

E. Influence of Nonlinear Term $[L^{c\text{-}s}]^{-1}$

To examine the effect of the induced inflow influence coefficient matrix, $[L^{c\text{-}s}(\alpha_n^m)]^{-1}$, on blade lag response and regressing lag damping, the following comparisons are made. First it is assumed that $[L^{c\text{-}s}(\alpha_n^m)]^{-1} = [L^{c\text{-}s}(\bar{\alpha}_1^0)]^{-1} = \text{const}$, i.e., $[L^{c\text{-}s}(\bar{\alpha}_1^0)]^{-1}$ is independent of time $\bar{t}$. $\bar{\alpha}_1^0$ is the steady uniform-induced flow obtained from the rotor momentum theory. Thus, the inflow influence coefficient matrix is constant in the numerical time integration process, i.e., in this process, the coefficient matrix is calculated only one time. These results are compared to those when $[L^{c\text{-}s}(\alpha_n^m)]^{-1}$ is dependent on $\bar{t}$.

Figure 11a shows a typical blade lag response at the tip for $\alpha_s = -3$ deg, $\mu = 0.26$, and $\theta_0 = 3$ deg. In Fig. 11a, the solid and broken lines indicate the results from without and with nonlinear consideration in the inflow influence matrix, respectively. It is found that the effect of allowing $[L^{c\text{-}s}]^{-1}$ to depend upon α_n^m is small. However, the difference in computational cost is significant, e.g., the CPU time using a SUN SPARC station 5 dropped from 5 h 37 min to 69 min 11 s. Figure 11b shows the regressing lag damping vs advance ratio, for $\theta_0 = 3$ deg, with $\alpha_s = -3$ deg. A comparison between the theory and experiment is also shown in Fig. 11b. The solid and broken lines indicate the results without and with nonlinear consideration in the inflow influence matrix, respectively. The ◇ symbols represent measured data. Again, the nonlinear effect is slight.

V. Concluding Remarks

A numerical simulation technique is applied to determine the transient response of a hingeless rotor model and to predict the lag damping and root flap moment for correlation with experimental results from a wind-tunnel test. Numerical investigations lead to the following conclusions:

The present theoretical/numerical method improves the correlation of the theoretical and experimental results over both earlier eigenvalues, perturbation analyses,[10] and the previous work,[8] using the uniform inflow 3 × 3 dynamic inflow models. The trim condition is important for obtaining a good experimental correlation. The results show that a better correlation of the trim conditions leads to a better lag damping correlation between the prediction and experimental data.

Unfortunately, the present method leads to many degrees of freedom in the nonlinear rotor system and, thus, large computational cost. For example, the CPU time using a SUN SPARC station 5 is 5 h and 37 min for a one flight condition. However, neglecting the nonlinearity in the aerodynamic influence matrix reduces the computational cost by a factor of 5, with only a slight loss in accuracy.

Acknowledgments

This work was supported, in part, under AFOSR Grant, "Limit Cycle Oscillations and Nonlinear Aeroelastic Wing-Response"; C. I. Chang and Brian Sanders were the Grant Monitors. The authors also thank David Peters for very helpful discussions of his work that have been the basis for our extension of his approach.

References

[1]Dowell, E. H., "A Simple Method for Converting Frequency Domain Aerodynamics to the Time Domain," NASA TM 81844, May 1980.

[2]Dinyavari, M. A. H., and Friedmann, P. P., "Unsteady Aerodynamics in Time and Frequency Domain for Finite Time Arbitrary Motion of Rotary Wings in Hover and in Forward Flight," *Proceedings of the AIAA/ASME/ASCE/AHS 25th Structures, Structural Dynamics, and Materials Conference*, AIAA, New York, 1984, pp. 266–282.

[3]Dinyavari, M. A. H., and Friedmann, P. P., "Application of the Finite-State Arbitrary Motion Aerodynamics to Rotor Blades Aeroelastic Response and Stability in Hover and in Forward Flight," *Proceedings of AIAA/ASME/ASCE/AHS 26th Structures, Structural Dynamics, and Materials Conference*, AIAA, New York, 1985, pp. 15–17.

[4]Friedmann, P. P., and Venkatesan, C.,"Finite State Modeling of Unsteady Aerodynamics and Application to a Rotor Dynamics Problem," 11th European Rotorcraft Forum, London, Sept. 1985.

[5]Gaonkar, G. H., and Peters, D. A., "Review of Dynamic Inflow Modeling for Rotorcraft Flight Dynamics," *Vertica*, Vol. 12, No. 3, 1988, pp. 213–242.

[6]Peters, D. A., and He, C. J., "Finite State Induced Flow Models, Part II: Three-Dimensional Rotor Disk," *Journal of Aircraft*, Vol. 32, No. 2, 1995, pp. 323–333.

[7]Tang, D. M., and Dowell, E. H., "Damping Prediction for a Stalled Rotor in Flap-Lag with Experimental Correlation," *Journal of the American Helicopter Society*, Vol. 40, No. 4, 1995, pp. 79–89.

[8]Tang, D. M., and Dowell, E. H., "Damping Prediction for a Hingeless Rotor Aeroelastic Stability with Experimental Correlation," *Journal of Aircraft*, Vol. 33, No. 6, 1996, pp. 1071–1078.

[9]McNulty, M. J., "Flap-Lag Stability Data for a Small Isolated Hingeless Rotor in Forward Flight," NASA TM 102189, Aug. 1989.

[10]Maier, T. H., Sharpe, D. L., and Lim, J. W., "Fundamental Investigation of Hingeless Rotor Aeroelastic Stability, Test Data and Correlation," American Helicopter Society 51st Annual Forum, May, 1995.

[11]Peter, D. A., "Toward a Unified Lift Model for Use in Rotor Blade Stability Analysis," *Journal of the American Helicopter Society*, Vol. 30, No. 3, 1985, pp. 32–42.

[12]Petot, D., "Differential Equation Modeling of Dynamic Stall," *Recherche Aerospatiale*, Vol. 5, No. 5, 1989, pp. 51–64.

[13]Hodges, D. H., and Dowell, E. H., "Nonlinear Equations of Motion for the Elastic Bending and Torsion of Twisted Nonuniform Rotor Blades," NASA TN D-7818, Dec. 1974.

[14]Pitt, D. M., and Peters, D. A., "Theoretical Prediction of Dynamic Inflow Derivatives," *Vertica*, Vol. 5, No. 1, 1981, pp. 21–34.

[15]Dunn, P., and Dugundji, J., "Nonlinear Stall Flutter and Divergence Analysis of Cantilevered Graphite/Epoxy Wings," *AIAA Journal*, Vol. 30, No. 1, 1992, pp. 153–162.